ERUPTION OF A MULTIPLE-TURN HELICAL MAGNETIC FLUX TUBE IN A LARGE FLARE: EVIDENCE FOR EXTERNAL AND INTERNAL RECONNECTION THAT FITS THE BREAKOUT MODEL OF SOLAR MAGNETIC ERUPTIONS

G. ALLEN GARY and R. L. MOORE
Marshall Space Flight Center, SD50, Huntsville, AL 35812
Allen.Gary@nasa.gov, Ron.Moore@nasa.gov

"la représenter avec une structure spirale" – P. A. Secchi[1]

Short Title: EVIDENCE FOR EXTERNAL AND INTERNAL RECONNECTION

---

[1] Secchi (1870) reports an observation by Major James Francis Tennant of a spiral structure prominence in the corona during the total eclipse of June 18, 1860.

ABSTRACT

We present observations and an interpretation of a unique multiple-turn spiral flux tube eruption from AR10030 on 2002 July 15. The TRACE CIV observations clearly show a flux tube that is helical and that is erupting from within a sheared magnetic field. These observations are interpreted in the context of the breakout model for magnetic field explosions. The initiation of the helix eruption starts 25 seconds after the peak of the flare's strongest impulsive spike of microwave gryosynchrotron radiation early in the flare's explosive phase, implying that the sheared core field is not the site of the initial reconnection. Within the quadrupolar configuration of the active region, the external and internal reconnection sites are identified in each of two consecutive eruptive flares that produce a double CME. The first external breakout reconnection apparently releases an underlying sheared core field and allows it to erupt, leading to internal reconnection in the wake of the erupting helix. This internal reconnection heats the two-ribbon flare and might or might not produce the helix. These events lead to the first CME and are followed by a second breakout that initiates a second and larger halo CME. The strong magnetic shear in the region is associated with rapid proper motion and evolution of the active region. The multiple-turn helix originates from above a sheared-field magnetic inversion line within a filament channel, and starts to erupt only after fast breakout reconnection has started. These observations are counter to the standard flare model and support the breakout model for eruptive flare initiation. However, the observations are compatible with internal reconnection in a sheared magnetic arcade in the formation and eruption of the helix.

Subject headings: Sun: flares — Sun: magnetic fields — Sun: coronal mass ejections — Sun: activity — Sun: Corona

1. INTRODUCTION

The complex event and structures of the X3 solar flare of 2002 July 15, 20:04 UT, have been discussed in a recent letter by Lui et al. (2003) in the context of an erupting flux rope model. TRACE 160 nm observations captured the ejection of a multiple-turn helical flux tube from a sheared magnetic field, which is a major signature of the standard model of eruptive flares (EFs). However, here we find this event, which produced a fast coronal mass ejection (CME), to have all the features required by the breakout model of magnetic field explosions. This is compatible with the erupting helix because the helix represents a unique observation of an eruption of a low-lying highly sheared magnetic field, which is a central requirement of both the standard model and the breakout model and many flare models (i.e., Moore et al. 2001, DeVore and Antiochos 2000, Forbes & Priest 1995, Priest & Milne 1980, Birn & Schindler 1981, and Hood & Priest 1980). We observe that the "breakout" of remote flare brightening occurs before the "explosion" of the sheared and helical core magnetic field. This observation favors the breakout model for the initiation of this flare.

It is generally recognized that coronal mass ejections and eruptive flares (CME/EFs) are part of a single complex phenomenon which includes (i) stressed magnetic fields, (ii) a triggering event(s) for rapid reconnection, (iii) the eruption of the magnetic field, and (iv) the post-flare closure of the field. The least understood of all the components of CME/EFs is the triggering mechanism which switches on rapid reconnection. At the center of various models to explain CME/EF events, but playing different roles, is a stressed magnetic field requiring magnetic helicity. The observation and importance of helicity has become a prominent part of solar physics in the last decade. The new time-dependent, three-dimensional magnetohydrodynamics codes show specifically how a sheared magnetic field can form multiple-turn core fields of filaments (DeVore and Antiochos 2000).

Within an historical context, solar magnetic helicity extends back to a year after the Carrington-Hodgson white-light flare of 1859. P. A. Secchi (1870) reports an observation by J. F. Tennant of a spiral structure prominence in the corona during the total eclipse of 1860. The vortical patterns seen around sunspots with the first spectroheliograph led G. E. Hale to discover the magnetic field in sunspots (Hufbauer 1991). The early models of the Sun's internal magnetic field by H. W. Babcock used kinked twisted toroidal fields (Priest 1982). The highly twisted field of the 1946 June 4 erupting prominence led Anzer and Tandberg-Hanssen (1970) to model prominences with helical structures. Raadu and Nakagawa (1971) introduced force-free field solutions of coronal field due to the solutions being similar to the observed vortical chromospheric patterns. Mouschovias and Poland (1978) introduced a twisted model for coronal loops. Rust and Kumar (1996) observed a global correlation of the handedness of the coronal X-ray sigmoids. Observations of erupting sigmoids suggest that multiple-turn helices are unstable (e.g., Pevtsov, Canfield, & Zirn 1996). Now with the TRACE observations reported herein we have an excellent example of an erupting core field from the site of a sheared photospheric magnetic field and a chromospheric filament. Reconnection in such fields is proposed to be the main initiator of the eruption in the standard model of eruptive flares (Moore et al. 2001).

In Figure 1, a set of six 160 nm images from TRACE show the eruption of a multiple-turn helical field in our flare. Such an eruption from a sheared core field is crucial to the standard model. The emission in these images is mainly due to CIV. To illustrate that the erupting feature in these images is a helical flux tube, a simple three-turn helix was modeled to simulate the observed aspect and expansion. The results are shown as inserts in Figure 1 and reproduce the helical structure. The geometry of this model was specified using the fact that, at the time of the erupting helix, the active region AR10030 was located at E01° and N22° and, in the image plane, the helix's associated neutral line (L_b, Figure 2) made an angle of ~22° with a N-S line. Furthermore, defining the helix velocity vector as the time rate of change of the displacement vector of the center of the helix, then, in the image plane, the velocity vector is titled up 41° from the E-W, constant latitude line. Using this angle and assuming that the helix velocity vector is perpendicular the associated magnetic neutral line then the plane of the rising helix (as defined by the helix center line and its foot points) is calculated to be tilted 36° from the local heliographic vertical.

The helical flux tube is plainly defined in the TRACE rapid sequence of 16 images (cf., Lui et al. 2003). This clearly represents the creation of a DeVore-Antiochos (2000) helical field or the core-field eruption envisioned by Moore et al. (2001). Large-scale helical structures associated with CMEs have been inferred to be ubiquitous in pre-eruptive and eruptive prominences (Dere et al. 1999, DeVore and Antiochos 2000, Moore et al. 2001). The main point of the observations, which will be discussed in further detail below, is that the initiation of the helix eruption starts 25 seconds after the first peak of the impulsive-phase microwave gryosynchrotron radiation, implying the eruptive core field was not the initial reconnection/acceleration site. In Figure 2, the general magnetic field configuration is seen in the MSFC vector magnetogram (top panel, with the main components of the active region labeled) and in a MDI longitudinal magnetogram (bottom panel). This labeling will be referred to throughout the paper. In Figure 3, the site of the helix eruption is seen to be the site of a filament in a pre-flare Hα image. The filament is along the center N-S neutral line labeled L_b in Figure 2. The image in Figure 3 also shows the general complexity of the region.

Again, the important finding of this paper is that these observations are counter to the standard flare model and support the breakout model for the eruption onset. However, these observations support reconnection within a sheared magnetic arcade to yield the helical field lines. As we follow the events in the quadrupolar configuration of the active region, the internal and external reconnection sites will be identified which are associated with a double flare event and a double CME. External outbreak reconnection begins before the helix eruption and internal reconnection below it. These events give rise to a CME. After the field that opens in this CME recloses, a second episode of external breakout reconnection initiates a second and stronger halo CME. The strong magnetic shear of the region is associated with rapid proper motion and evolution of the active region. The multiple-turn helix originates from above a magnetic inversion line in the sheared magnetic field in a filament channel, but starts to erupt only well after breakout as been initiated.

Section II of this paper describes (i) transition region and chromospheric images that show the eruptive helix and the sites of enhance emission (heating), (ii) the photospheric magnetic field that leads to an understanding of the three-dimensional field configuration,

(iii) the time profiles of the X-ray and microwave data that mark the events, and (iv) the observations of the two coronal mass ejections that certify the global magnetic outbreak. The many observations from the various solar instruments reveal the nature of the event in detail. Section III presents the analysis of the configuration of the magnetic field and characterizes the physical properties of the erupting helix. Section IV summaries the analysis and presents a schematic model that fits the observations. In particular we consider the multiple-turn helical magnetic flux tube within a sheared magnetic field and its context within the breakout model for magnetic field explosions. The role of the external and internal reconnection in the destabilization of the active region's magnetic field is discussed.

2. OBSERVATIONS

There are ample observations to give the general nature of the magnetic field topology associated with the event. The quadrupolar magnetic components of the region are labeled on the vector magnetogram (Figure 2), including three sheared-field segments of the magnetic neutral line (L_a, L_b & L_c). The erupting helix comes from over the neutral line L_b, and flare ribbons occur along each of the two sheared-field neutral lines (L_b & L_c) to the right of the preceding sunspot.

2.1. Transition Region and Chromospheric Images

On 2002 July 15, the Transition Region and Coronal Explorer (TRACE) instrument was in a 160 nm flare mode when an X3 X-ray flare in AR 10030 occurred. Details of the TRACE instrumentation can be found in Handy et al. (1999). The active region was observed throughout most of the day in a flare monitoring mode with 768x768 pixels of a spatial resolution of 0."5. The total image count for the day was 6005. For the period of 20:00 to 20:03 there are 48 images with 768x768 pixels, and after 20:02:59 UT there are 828 images with 512x512 pixels of spatial resolution 0."5, and a temporal cadence of every 2 seconds. The UV continuum 160 nm images capture the two-ribbon flares and other regional brightenings. The spectral response of the 160 nm filter (24.5 nm FWHM) peaks near 155 nm and captures the strong CIV resonant line pair emission (2s-2p, 154.82 and 155.08 nm) from the transition region at 100,000 K in the flaring stage; the background quite-sun emission is from photoionization of Si ($3p^2$ ^3P) around the temperature minimum region (Handy et al. 1998, Qui, et al. 2000, Cuny 1971). For an X3 flare, the CIV radiance (specific intensity) brightens a factor of more than 3400 (Brekke et al 1966); hence the CIV emission dominates the emission after 20:03 UT until after 20:30. (We refer herein to these images as CIV images; but, these are not the reduced CIV TRACE images obtained by the method of Handy et al. (1998).) During the preflare phase, TRACE captures transient brightens probably related to flux emergence, flux cancellation, and less dramatic magnetic field restructuring. The images show the helix eruption starting at 20:04 UT, ~one minute into the flare according to the NOAA flare listing. The eruption occurs on the eastern side of the leading spot (P_1). The TRACE team reports that "the region was so bright that TRACE reduced the exposure times to as little as 1/625 seconds starting at 20:03 UT; the result is that the background emission disappears entirely and only detector and data-compression noise is seen outside the

bright flare kernel for a while, until exposure times become longer than 1/150 seconds after 20:07:28 UT.''

In Figure 1, the multiple-turn helix is seen erupting from a site of sheared magnetic field. These TRACE sub-arrays have a field of view of 125 arcsec located between the positive sunspots (P_1 & P_3) (cf. Lui et al. 2003). Figure 5 shows that the eruption starts at ~20:04:17 UT and accelerates at 25 km s^{-1} during the first 30 s. The helix clearly has three turns as seen at 20:04:51 UT; however at 20:04:34 UT there are indications of perhaps five bright knots in the early phase of the eruption. In the TRACE observations of this eruption containing 39 frames taken every two seconds, both legs of the helix are seen with the leg to the southwest showing an untwisting action. The base length of the helix is 3.9×10^4 km as measured from foot to foot. From 20:04:51 UT, the loop begins to disappear and identification of the turns is impossible. In Figure 1 (inserts), a simple model of an erupting helix of 3 turns simulates the time period of 20:04:23-20:04:51 UT. Shown with the same appropriate aspect angle of the CIV observations of the helix eruption, this simulation has a semi-circular shaped helix rising with the legs of the flux tube fixed to two 'photospheric' foot points. Because of the aspect angle and the bowed central core, each of the loops has a V-cusp shape towards the originating neutral line and a rounded top (cf., with the inserts). The V-cusps are seen in the TRACE observations. Introducing unwinding by a time dependent reduction of the number of turns, the apparent spinning motion of helix legs, as seen in the southwestern leg of the TRACE helix, can also be simulated.

The results of the velocity calculations for the erupting helix are shown in Figure 5. The transverse velocity motion across the image plane (solid upper curve), initially has a constant acceleration (dash-dotted line) of ~25 km s^{-2}. The transverse velocity was obtained from measurements of the displacements of the apex of the core of the helix. The radial expansion of the helix from its core has a velocity of ~185 km s^{-1} after about 15 seconds. The radial expansion was measured using the average semi-diameter of the main turns. Extrapolation of the transverse velocity to zero gives an onset time of t(0)= 20:04:17 UT. The times of the first five images of Figure 1 are marked A-E in Figure 5. At the time of each image, the vertical lines are the error (200 km s^{-1}) associated with the transverse velocity; the helix expansion velocity has the same uncertainty.

TRACE CIV images of key events in the X3 flare are shown in Figure 4. The field of view (FOV) here is 6.'8x6.'8, i.e., ~3x FOV of Figure 1. At 19:49:58 and 20:02:53 UT the emission features E_1, E_2, E_3, & E_4 are located at separatrix sites. The first eruption produces the two flare ribbons R_1 (shown at 20:05:02 UT) across the sheared-field neutral line L_b. At 20:28:01, a second eruption is producing the two flare ribbons R_2 across the sheared-field neutral line L_c. At 20:28:41 UT, an upper atmospheric coronal separatrix (S) is seen; from the movie it is clear that this feature is in the lower corona. In the later phase of the flare, at 20:41:58 UT, the reconnection associated with re-closing of the field again brightens separatrix sites E_1' and E_4'. The main neutral line (thin line) is from the MDI longitudinal magnetogram (Figure 2, bottom panel).

Chromospheric images in Hα were obtained by Big Bear Solar Observatory in the preflare time frame and during the flare by the U.S. Air Force Solar Optical Observing Network (SOON) observatories at Holloman AFB and Learmonth, Australia. SOON Hα images show remote Hα flare brightenings (at E_1, E_2, E_3, and E_4) at 20:02:25 UT, near the start of the impulsive phase (in the rise of the microwave peak r_1). Following this, the

SOON images show the development of the two-ribbon flare bracketing neutral line L_b. In Figure 3, a Learmonth Hα image (05:42 UT) shows well the filaments associated with neutral line segments L_a, L_b and L_c. The filaments of the neutral lines L_b and L_c return after the event; they are as seen again early on July 16.

2.2. Vector and Longitudinal Magnetograms

On 2002 July 15, the Marshall Space Flight Center (MSFC) solar vector magnetograph obtained a set of magnetograms of AR10030 which showed strong magnetic shear along the neutral lines. The field of view of the instrument is 7 x 5½ arcmin (328x258 obtained by 2x2 binning of 0.64 arcsec pixels). Seven vector sets were obtained between 17:18 and 18:03 UT: 4 sets were taken at 9 pm to the blue of line center, 1 set was at 9 pm to the red of line center, 1 set for photocalibration, and 1 set for dark-current calibration. Each set has coaligned Hα images. The photospheric vector magnetograms, obtained from the FeI Zeeman line at 525.02 nm, measure the nonpotentialilty of the region. In particular they show the high magnetic shear along the neutral line in the active region.

In Figure 2, the MSFC vector magnetogram shows the strongly-sheared nonpotential field along the three segments L_a, L_b and L_c of the main neutral line. The photospheric magnetic contour levels are ± 1000, 700, 400, 50, 10 G. The transverse field vectors are shown as dashes. Highly-sheared (shear angle > 45°) transverse magnetic field along neutral lines is correlated with CME events (Falconer, Moore, & Gary 2002). In this figure, the background is the photospheric brightness in the FeI 525.02 nm line.

On the ESA/NASA Solar and Heliospheric Observatory (SOHO) satellite, the Michelson Doppler Imager (MDI) obtained full-disk longitudinal photospheric magnetograms using the NiI Zeeman line at 676.78nm. The 1024x1024, 60 sec cadence, full-disk magnetograms, having 4."0 spatial resolution and ~50G uncertainty, were used to investigate the dynamic movement of several magnetic features during the day. The full-disk (level 1.5/reformatted and calibrated) images at 60 sec cadence were obtained in the time intervals 00:00-05:40 UT, 11:04-12:35 UT, 13:52-13:59 UT, and 14:00-14:28 UT, with additional observations at 16:00, 17:36, 19:12, 20:48, and 22:24. The MDI image magnetograms show eastward motion of F_3 relative to P_3. This and other motions within the complex continuously change the stressed global magnetic field. MDI also provided high-resolution images of the active region having 11.'0 x11.'0 field of view and 1."25 spatial resolution. For July 15, high-resolution MDI magnetograms were obtained around 10:54 and 13:41 UT. For the high-resolution images, the center of the field is displaced 160 arc-sec to the north of the center of the full-disc field in the usual orientation and captured AR10030 at N22 E01 on 2002 July 15. In Figure 2 (bottom panel), the high-resolution MDI magnetogram at 10:56 UT shows the details of the principle sunspots, magnetic islands, and neutral lines. The small bipolar delta region (P_2 & F_2) develops at the southern end of L_b during the day of July 15; and at the northern end another small bipolar region developed as was pointed out by Lui et al. (2003).The second, lower sunspot of P_3, moves rapidly (0.19 km s^{-1}) to the west during the day, with respect to the main spot of P_3. There are 0.12 arcsec images and movies of the region from the Swedish 1-m telescope, but the field of view only captures the sunspot P_3 (Scharmer et al. 2002).

2.3. X-ray and Microwave Time Profiles

The Geostationary Operational Environmental Satellite (GOES-8) observed the soft X-ray emission of the X3.1 flare with 1-min time resolution. The full disk integrated X-ray flux as a function of time during the time period of 19:00-21:00 UT, observed in the 0.05-0.4 nm and 0.1-0.8 nm channels, is shown in Figure 7. The main peak (X3.1) at g_1=20:07 UT and a secondary peak at g_2=20:28 (M4.1) were produced by the two ejective flare events in AR 10030.

The Owens Valley Radio Observatory (OVRO) Solar Array (OVSA) obtained multifrequency microwave emission in the 1-18 GHz range at an 8-sec temporal resolution. This microwave emission is gyrosynchrotron radiation that is produced by the same population of the electrons that produce the 10-100 keV hard X-ray bremsstrahlung emission in the impulsive phase of flares (Gary 2000). There are four main microwave bursts occurring at r_1=20:03:52, r_2=20:11:20, r_3=20:18:36, and r_4=20:24:12 UT; and the bursts have a typical full-width half maximum (FWHM) time durations of ~2-4 min, as determined from the 10 GHz profile. The OVSA 10 GHz microwave power flux is plotted with the GOES data in Figure 7. We note with regret that only the decay phase of the X flare of July 15 was seen by Ramarty High Energy Solar Spectroscopic Imager (RHESSI) due to Earth occultation; hence the initial phase timings were missed by RHESSI.

2.4. Coronagraph Images

Associated with the X3 flare of AR 10030, the Large Angle and Spectrometric Coronagraph (LASCO/SOHO) observed the first coronal mass ejection (CME) event on July 15 at 20:30 UT and the second CME about a half hour later. The second CME was initially observed as a bright front off the northeast limb and as a full halo CME by 22:30 UT. The halo is fainter in the south, and is seen there only in the difference images. The LASCO team reported that the front moved fast (~1100 km/s) and had some trailing material mainly in the northeast. The C2 coronagraph (2-6 R_s), with 23."0 spatial resolution, recorded strong CME emission in the northeastern corona between 20:30 and 22:30 UT. The C3 coronagraph (3.7-32 R_s) difference images, with 112."0 spatial resolution, show the CME from 21:18 UT (July 15) to 03:18 UT (July 16) as a halo CME. In Figure 8, a difference image shows the second CME as seen by LASCO C3 at 02:18 UT on July 16. A weak halo is seen opposite the main emission.

2.5 Chronology of Events

According to the GOES and OVSA time profiles (Figure 7), the eruption events started at 20:02 UT with preflare X-ray activity starting 19:45 UT. Below we list the chronology of the events associated with the July 15th X3 flare, helix eruption, and CME eruptions:

      19:45 UT.   — Preflare X-ray emission begins.
      19:50 UT.   — Transition region CIV emission is seen at footpoints of the
                  separatrix.

20:02 UT.　　— X-ray impulsive phase begins with enhanced CIV and Hα ribbons brightening at separatrix feet.
20:03:52 UT — First microwave burst r_1 from 10-100 keV electrons peaks.
20:04:17 UT. — Twenty-five seconds after r_1 peaks, the CIV helix begins to ascend. First set of CIV ribbons (R_1) across L_b start to form.
20:05 UT.　　— Helix disappears and flare R_1 ribbons are fully formed in CIV and Hα.
20:07 UT.　　— Peak of the GOES X-ray flux (X3.1, 0.1-0.8nm channel)
20:11:20 UT. — Second microwave burst r_2 from 10-100 keV electrons peaks.
20:18:36 UT. — Third microwave burst r_3 from 10-100 keV electrons peaks.
20:24:12 UT. — Fourth microwave burst r_4 from 10-100 keV electrons peaks.
20:26 UT.　　— The second set of CIV ribbons (R_2) has formed across L_c which is a separate site from the first flare ribbons (R_1).
20:28UT.　　— Secondary peak of the GOES X-ray flux (M4.1, 0.1-0.8nm channel).
20:29 UT.　　— Coronal separatrix is seen in CIV.
20:30 UT.　　— First CME is seen in LASCO C2 in the northeast.
20:41 UT.　　— Two remote CIV emission patches (E'_1 and E'_4) have brightened.
22:18 UT.　　— Second CME is first seen in LASCO C3 difference images.
23:18 UT.　　— Second CME is seen as a halo event in LASCO C3 difference images.
02:18 UT. (July 16) — Second CME reaching 25 R_s and seen as a halo event.

3. ANALYSIS

The solar eruptions of July 15 will be analyzed in terms of the magnetic configuration and external and internal reconnection. In this section we will discuss (i) the magnetic morphology as determined by magnetograms and their extrapolation, (ii) a step by step scenario of the emissions and timing of the CIV and chromospheric features seen in the data, and (iii) the dynamical formation of the TRACE helix in relation with the DeVore-Antiochos (2000) MDH calculations, and the velocities of the erupting helix. The observation of the eruption of the helix from a sheared core field is of particular importance.

3.1 Magnetic Morphology

A set of potential field lines are shown in Figure 6; these were computed from an MDI magnetogram taking the region viewed in the magnetogram to be a flat plane. The potential field is used to show the topology of the nonpotential quadrupolar complex. A set of field lines (white lines) are specifically associated with the region enclosing the negative field of F_1. The outer extremities of this set of field lines define the separatrix cupola. The influence of the small magnetic delta dipoles (e.g., P_2 & F_2) is negligible on the overall quadrupolar field. The height in the side view is 140 Mm. At this height the plasma beta is ~1 (Gary 2001). Hence, the magnetic field is influenced by the (unknown) upper boundary conditions and this current-free-field calculation models only the general

connectivity to be expected, i.e., the topology. The exact conjugate foot points are not modeled by this field. However, the morphology of the potential field reflects the general morphology of the region. In the upper panel of Figure 6, the set of field lines plotted start on a line that is roughly the axis of symmetry of the region. This model emphasizes the null above the region F_1 by having the field lines associated with F_1 in white. The appropriate upper boundary conditions are unknown and are not included in the calculation. It is probable that breakout reconnection at the null initiates the eruption of the sheared field along the neutral line L_b, and in a second episode, initiates the eruption of the sheared field along the neutral line L_c.

In Figure 10, on the left, the enlargement shows the TRACE image at 20:28:41 UT extracted from Figure 4. Here the separatrix feature is that of an inverted-Y null located in the corona above the negative region F_3. From the CIV movie it appears that this null is not the null of the potential field, but is the null at the base of the reclosing-reconnection current sheet in the wake of the second eruption. This separatrix region appears be filled with material from the eruption that produces the second two-ribbon flare. An illustration of the event is shown on the right with a set of field lines defining the separatrix. Filippov (1999) points out that null points are usually assumed to be sites of reconnection. However, in an observation of a three-dimensional null point, he reports that there appears no significant heating associated with the null point. It may be that the heating at our null is transient and highly nonuniform, allowing the separatrix to be seen in CIV, as in this image.

3.2 Scenario of Flare Evolution

In Figure 4, TRACE CIV images of the key events associated with the X3 flare are shown. The impulsive phase of the flare begins at 20:02 UT. However in the preflare stage there are small brightens at four separatrix footpoints (Panel 1 of Figure 4). At 19:49:58 UT, the emission at E_1, E_2, E_3 and E_4 is at the locations of separatrix foot point sites connected to the null above F_3 (cf., Figures 6 and 9). Slow breakout reconnection is beginning at the null.   At 20:02:53 UT the separatrix emission E_1, E_2, E_3 and E_4 is now brighter from the particles and heat from the fast reconnection of the outbreak. In Hα at 20:03:55 UT and in CIV at 20:05:02 UT (Figure 4), the pair of flare ribbons R_1 across the sheared neutral line L_b is growing. These flare ribbons are heated from internal reconnection in the wake of the erupting helix. The eruption of the helix and the reconnection below it are consequences of the external breakout reconnection, which releases the sheared cored filed to erupt and reconnect internally.   At 20:28:01 UT, a second eruption is producing the two flare ribbons R_2 across the sheared neutral line L_c. This eruption is released by a second episode of breakout reconnection at the null. This breakout reconnection begins once the reclosing and reforming reconnection of the first eruption sufficiently erodes the envelope of field in which the sheared core field along L_c recsides. At 20:28:41 UT, an upper atmospheric coronal separatrix (S) is seen filled with the material released by the eruption from over L_c. At 20:41:56 UT, the reconnection re-closing of the field opened by the second eruption produces the brightenings at E'_1 and E'_4, near the former separatrix feet E_1 and E_4.

In Figure 9, six stages of the scenario for the double-flare, double-CME event of July 15 are shown. In panel 1, the preflare, stressed, quadrupolar magnetic field configuration is illustrated with magnetic fields concentrations P_1, F_1, P_3, & F_3, the separatrix foot locations E_1, E_2, E_3, & E_4, the sheared-field neutral lines L_a, L_b, & L_c, and the X-type neutral point. In panel 1, the two dots indicate which field lines are next to be reconnected as the stressed field (thick field line) over L_b pushes outwards. The slow reconnection at the X-point feeds energy to heat the separatrix regions. The points E_1-E_4 are the intersection of the separatrices (shown in light gray) with the photosphere. The magnetic topology shown here has been simplified; as seen in Figure 4, the E_4 emission is outside of the plane shown and its connection to the null might be better represented by a spline of field lines (cf., Aulaner et al. 2000). The configuration of panel 1 is for a time of ~19:50 UT and the times for the other panels are near or between the times of the TRACE images in Figure 4.

As the magnetic field evolves through stress relief above the neutral line L_b, progression of the reconnection at the X-point and the resulting expansion of the sheared core field move the X-point upwards. As the process precedes the separatrix emission increases. Following Antiochos (1998), breakout reconnection transfers flux to the two side lobes of the quadrupole, removes the confining field, and thus unleashes the sheared core field to erupt. The breakout high over L_b either allows the pre-formed helix to erupt or allows the helix to form and erupt via internal reconnection, as illustrated in panel 2. The opening of the quadrupolar field by this breakout eruption is confirmed by the first CME. The reclosing reconnection along the current sheet above the Y-point null in panel 3 powers the two-ribbon flare R_1 across the neutral line L_b. This reclosing reconnection also powers the second and third microwave spikes, and produces the first maximum in the soft X-ray flux.

In panel 4 the reclosed field configuration is shown well after the first breakout but before the second breakout event. The second breakout event is produced by the expanding stressed field over L_c. The dots at the X-point in panel 4 show the reconnection direction for this second breakout, which follows a similar, but not identical, scenario to panel 2. Due to the stressed magnetic field and the removed overlying magnetic loops by reconnection in the aftermath of the first breakout event, the flux over L_c expands outward. With rapid reconnection on the east side of the expanding breakout, the stressed flux associated with Lc erupts outward forming a current sheet behind and a current sheet on its east side. The result of this eruption is the configuration of panel 5. This breakout eruption is manifested by the fourth microwave burst r_4 at 20:24 UT, the second filament eruption, and the beginning of the second two-ribbon flare (R_2). The opening of the quadrupolar field the second time, i.e. the second breakout, is confirmed by a second and faster CME. The second CME is faster perhaps due to a weakened field configuration resulting from the first breakout. As this configuration relaxes the inverted-Y separatrix above F_3 is seen in the TRACE images at 20:28UT (Figure 10.) The final-phase reclosing reconnection is shown in the panel 6. This final reclosing reconnection above the late-phase high Y-point null produces the heating for E'_1 and E'_4, which is seen in the last panel of Figure 4 at t=20:41:56UT.

3.3 Formation and Eruption of the Helix

The tether-cutting concept is at the heart of the standard model for eruptive flares as first proposed by Hirayama (1974) and extended recently by Moore et al. (2001). The concept is that reconnection begins low in the sheared core of a magnetic arcade. This tether-cutting reconnection progressively transfers magnetic shear from low to higher in the arcade, producing a growing twisted flux tube and unleashing it to erupt. This configuration is normally assumed responsible for the sigmoid-shape X-ray signatures. Antiochos & DeVore (2000) state that there are no three-dimensional simulations that show evidence of such tether-cutting reconnection. However, we believe that the TRACE helix was formed by such reconnection if the helix was not formed before it erupted. The question is whether this rapid tether-cutting reconnection of the standard model is the initiator of our CME/EFs. An alternative model for the eruptive flare trigger is the "breakout" model (Antiochos 1998, Antiochos, DeVore, & Klimchuk 1999). The key features of this model are (1) multi-polar configuration, (2) photospheric shearing, and (3) rapid reconnection *high* in the corona. The important distinction is that the breakout model trigger or magnetic destabilization is by external reconnection high in the corona and not within the stressed core field. Therefore the global magnetic field and higher plasma beta are more important than in the standard model.

The helix is formed in a strongly sheared magnetic field along neutral line L_b. We do not believe that a twisted flux tube undergoes kink instability to form the multiple-turn helix. If the helix is formed before it erupts, we think that it is more likely that its formation follows the development of the three-dimensional MHD simulation described by DeVore and Antiochos (2000). Since the birth site of the helix is in a sheared magnetic field and the overall active region is evolving with moving magnetic elements pouring out of sunspot P_3, this subregion along L_b has the necessary character for the DeVore-Antiochos model. A sheared-core arcade field, through gradual internal reconnection, becomes a multiple-turn helix straddling the neutral line. This pre-eruption sheared field with helical core remains stable until the overlying field is sufficiently weakened by the external breakout reconnection, and then erupts and produces a CME.

The characteristics of the helix in terms of its transverse and radial velocity are given in Figure 5. We now compare the observed erupting velocities with the Alfven speed, the propagation speed of magnetic disturbance. The maximum transverse velocity perpendicular to the line of sight was 800 km s^{-1}, while the maximum radial expansion was 185 km s^{-1}. From the geometry discussion in section §1, the velocity is tilted at ~45° away from the image plane; hence the helix velocity is ~ 1100 km s^{-1}. The Alfven velocity, V_a, is given by (cf. Mann et al. 2000)

$$V_a = B/(4\pi\rho)^{1/2} = B/(4\pi\ \xi\ m_p\ N)^{1/2} = 2.03 \cdot 10^{11}\ B/Ne^{1/2}, \qquad (1)$$

for full particle number density $N = N_e/0.52$, $\xi = 0.6$, and $m_p = 1.67 \cdot 10^{-24}$ gm; or equivalently (cf. Allen 2000):

$$V_a = antilog_{10} \{ 11.3 - log_{10}(N_e[cm^{-3}])/2 + log_{10}(B[G]) \cdot 10^{-5} \}\ km\ s^{-1}. \quad (2)$$

Because of the observational difficulties of the obtaining the magnetic field above the photosphere, the height dependence of the magnetic field is uncertain. We consider a range of magnetic field strength from 10 and 100 G. For the transition region number densities of $N_e = 10^9$ [or 10^{10}] cm^{-3} (cf. Vernazza, Avrett, & Loeser (1981), models C and P), the Alfven velocities for B=100 G [or 10 G] are V_a= 630 [or 200] km s^{-1} and V_a= 6300 [or 2000] km s^{-1} . From these densities and magnetic field values for the helix which are uncertain but reasonable, we conclude the helix velocities are physically

consistent with field strength of 10 to 100 G. Using the helix acceleration (Figure 5) and correcting for the aspect angle (§1), the helix's estimated height is ~9000 km after 30 seconds. The Newkirk model gives a density at this height of $N_e=10^{8.89}$ cm^{-3} (Mann et al. 2000); using B=22 G, the Alfven velocity is V_a~1500 km s^{-1}. These higher Alfven speeds are physically consistent with the speeds of the helix and the CMEs. Furthermore, assuming that the plasma in the helix is propelled by the magnetic field, and equating the magnetic energy density $B^2/8\pi$ and the kinetic density $\frac{1}{2}mv^2$, one obtains an estimate of the magnetic field strength of $B=4.5\times10^{-12}$ v n$^{\frac{1}{2}}$ G (Tandberg-Hanssen et al. 1980). For a velocity of 500 km s^{-1} and particle density of $n=10^{10}$ cm^{-3}, the estimated magnetic field of 20 G is consistent with the values of the Alfven velocities. The conclusion of these estimates is that the observed velocities have reasonable magnitudes and are consistent with the observed strength and configuration of the magnetic field.

4. SUMMARY AND DISCUSSION

The relation between core-field tether cutting and global magnetic ballooning via breakout in initiating the magnetic eruption is answered for the case studied. The specific timing of the eruption of a core field is seen from the TRACE images which capture the eruption of the core field helix. This eruption begins after the initiation of the flare. This supports the breakout model over the standard model for the initiation of the X3 flare of 15 July 2002 (20:02UT).

The ejections of twisted prominences have been seen on the limb since 1860. The classic example is the 1946 June 4 "Grandpa" event (Gibson, 1973). On the disk, where the magnetic field configuration can be clearly identified, observed eruptions of helical filaments are fewer, but they exist. An example of such is the event reported by Kurokawa et al. (1987); they reported Hα observations of a helical eruption from AR 4474 on 1984 April 25. This helical eruption is similar to the TRACE helix in that the eruption is after the impulsive phase of the flare and is from a sheared magnetic field. Over a period of 22 minutes a highly twisted helical filament is seen to erupt and untwist from the delta sunspot configuration, after the X13 flare which occurred at 00:01UT. The impulsive phase started 4 min *before* the filament started to erupt. In the blue-wing Hα images, the filament was seen for 4 min after it lifted off and one leg became detached. This example also suggests that the standard model must be in error for the initiation of this flare.

In the breakout model as described by Antiochos, Devore, and Klimchuk (1999) a complex magnetic field configuration resides within an overarching magnetic field such that a null point resides high above a neutral line. The photospheric magnetic field across the neutral line becomes stressed by foot point motion. The stressed magnetic field pushes outwards and the null rises. As the null moves outward, it reaches or obtains a high-β condition. The expansion of the stressed inner flux system compress the high-β region about the null until the dissipation length scale is reached and rapid reconnection is triggered.

The importance of our observations and the Kurokawa et al. observations is that they distinguished between the two competing models. The observations of the 2002 July 15 flare support the breakout model endorsed and developed by S. K. Antiochos for initiation of eruptive flares (Antiochos, DeVore, & Klimchuk 1999). First, our

observations show that the eruption of the sheared helix core of stressed magnetic field begins after the impulsive phase has started. This is in conflict with the standard model and supports the breakout model. Second, the initial brightenings are distant from the neutral lines and agree with reconnection at the null and associated separatrix-cupola footpoints. Third, the magnetic field is a complex quadrupolar field that is undergoing evolution. There are several other important points to make in regards to the breakout model and our observations. Antiochos et al. (1999) makes the case that the energy for CMEs must be stored in the stressed magnetic field of a multiple flux system. The quasi-static evolution of the stress magnetic field is driven by displacement of magnetic foot points and the emergence-submergence of magnetic flux. The MDI movie of the complex AR 10030 shows such strong activity in the photospheric magnetic flux distribution. Within the model, the sheared field expands outwards and pushes overlying flux (and the null point) outward. AR 10030 is indeed highly stressed as shown by the MSFC vector magnetograms. Gary (2001) points out that the plasma-β begins to increase and approach 1 at relatively low coronal heights (100 Mm) over active regions, i.e., the force-free region is rather low in the corona. This implies that the plasma at the X-point can inhibit the onset of reconnection until the current sheet becomes very thin. Also important to the breakout model is that much of the flux of the central and overlying systems remains closed. This is consistent with the X3 flare. In the breakout model, intense current sheets form late in the shearing; this is consistent with having observed highly sheared magnetic fields for hours before flare onset.   From the timing of the two eruptions form the two neutral lines L_b and L_c and the timing of the two CMEs, the plasma within the two CME must come from the eruptions associated with the two two-ribbon flares. However, the most decisive observation is that the initial impulsive phase occurred before the first core eruption.

   In conclusion, we feel that these observations show that the standard model for the initiation of eruptive flares does not apply to all ejective flares. However, the upper reconnection site of the breakout has yet to be directly observed. The trigger site of flares is still elusive.

Observatory and Owens Valley Radio Observatory Solar Array is maintained and operated by the Center for Solar Research at New Jersey Institute of Technology.

REFERENCES

Allen, C. W. 1973, Astrophyiscal Quantities, Athlone Press, London

Allen, C. W. 2000, Astrophyiscal Quantities, Athlone Press, London

Antiochos, S. K. 1998, ApJ, 502, L181

Antiochos, S. K., DeVore, C. R., & Klimchuk, J. A. 1999, ApJ, 510, 485

Antiochos, S. K., & DeVore, C. R., 2002

Anzer, U., & Tandberg-Hanssen, E. 1970, Sol. Phys., 11, 61

Aschwanden, M. J., Newmark, J. S., Delaboudiniere, J-P., Neupert, W. M., Klimchuk, J. A., Gary, G. Allen, Portier-Fozzani, F., and Zucker, A., 1999, ApJ, 515, 842 (1999)

Aulanier, G., DeLuca, E. E., Antiochos, S. K., McMullen, R. A., and Golub, L. 2000, ApJ, 540, 1126

Birn, J., & Schindler, K. 1981, Solar flare magnetohydrodynamics, E. Priest (ed.), Gordon and Breach Science Publishers, New York, p. 337

Brekke, P., Rottman, G. J., Fontenla, J., and Judge, P. G. 1996, Astrophys. J., 468, 418

Bruls, J. H. M. J., Lites, B. W., & Murphy, G. A. 1991, in "Solar Polarimetry", ed. L. J. November, NSO/Sacramento Peak Summer Workshop XI, Sunspot, NM, p. 444-456

Cuny, Y. 1971, Sol. Phys., 16, 293

Demoulin, P., Mandrini, C. H., Rovia M. G., Henoux, J. C., & Machado, M. E. 1994, Sol. Phys., 150, 221

Dere, K. P., Brueckner, G. E., Howard, R. A., Michels, D. J., & Delaboudinier, J. P. 1999, ApJ, 516, 465

DeVore, C. R., & Antiochos, S. K. 2000, ApJ, 539, 954

Dulk, G. A., & McLean, D. J. 1978, Sol. Phys., 57, 279

Falconer, D. A., Gary, G. A., Moore, R. L., & Porter, J. G. 2000, ApJ, 528, 1004

Falconer, D. A., Moore, R. L., & Gary, G. A. 2002, ApJ, 569, 1016

Filippov, B. 1999, Sol. Phys., 185, 297

Fontenla, J. M., Avrett, E. H., & Loeser, R. 1990, ApJ, 355, 700

Forbes, T. G., & Priest, E. 1995, ApJ, 446, 377

Gary, D. E. 2000, High Energy Solar Physics Anticipating HESSI, R. Ramaty and N. Mandzhavidze (eds.), ASP Conference Series 206, 297

Gary, G. A. 2001, Sol. Phys., 203, 71

Gary, G. A., & Musielak, Z. E. 1992, ApJ, 393, 722

Gary, G. A. 1996, Sol. Phys., 163, 43

Gary, G. A. 1997, Sol. Phys., 174, 241

Gary, G. A., & Alexander, D. 1999, Sol. Phys., 186, 123

Gibson, E.   1973, The Quiet Sun, NASA SP-303, U. S. Government Printing Office, Washington, D. C., p.66

Gibson, S. E., & et al. 2002, ApJ, 574, 1021

Hagyard, M. J., Teuber, D., West, E. A., Tandberg-Hanssen, E., Henize, W, Jr., Beckers, J. M., Bruner, M., Hyder, C. L., & Woodgate, B. E. 1983, Sol. Phys., 84, 13

Handy, B. N., et al. 1998, Sol. Phys., 183, 29

Handy, B. N., et al. 1999, Sol. Phys. , 187, 229

Hiei, E., & Hundhausen, A. J. 1996, 'Development of Coronal Helmet Streamer of 24 January 1992', in Y. Uchida, T. Kosugi, and H. S. Hudson (eds.), Magnetodynamic Phenomena in the Solar Atmosphere - Prototypes of Stellar Magnetic Activity', Kluwer Academic Publishers, Dordrecht, Holland, 125-126

Hood, A. W., & Priest, E. R.1980, Solar Phys., 66, 113

Hufbauer, K. 1991, Exploring the Sun-Solar Science since Galileo, John Hopkins, Baltimore, Md.

Kano, R. and Tsuneta, S. 1995, ApJ, 454, 934

Kurokawa, H., Hanaoka, Y., Shibata, K, & Uchida, Y. 1987, Sol. Phys., 108, 251

Lee, J., White, S. M., Gopalswamy, & Kundu, M. R. 1997, Sol. Phys., 174, 175

Lui, Y., Jiang, Y., Ji, H., Zhang, H, & Wang, H. 2003, ApJ, 593, L137

Mann, G., Aurass, H., Klassen, A., Estel, C, & Thompson, B. J. 2000, 8th SOHO Workshop Plasma Dynamics and Diagnostics in the Solar Transition Region and Corona. Eds J.-C. Vial and B. Kaldeich-Schümann., ESA Special Publications 446, 477

Moore, R. L., Sterling, A. C., Hudson, H. S., & Lemen, J. R. 2002, ApJ, 552, 833.

Mouschovias, T. C., & Poland, A. I. 1978, ApJ, 220, 675

Pevtsov, A. A., Canfield, R. C., & Zirin, H. 1996, ApJ, 473, 533

Priest, E. R. 1982, Solar Magnetohydrodyanmics, Reidel, Boston, Mass.

Priest, E. R.; Milne, A. M. 1980, Sol. Phys., 65, 315

Pneuman, G. W., & Kopp, R. A. 1971, Sol. Phys., 18,258

Qiu, J., Ding, M. D.,Wang, H. , Denker,C., & Goode, P. R., 2000, ApJ, 544, L157

Raadu, M. A., & Nakawaga, Y. 1971, Sol. Phys., 20, 64

Rosner, R., Tucker, W., & Viannia, G. 1978, ApJ, 220, 643 (RTV)

Rust, D. M., & Kumar, A. 1996, ApJ, 464, L199

Scharmer, G. B., Gudiksen, B. V., Kiselman, D., Lőfdahl, M. G., & Rouppe van der Voort, L. H. M. 2000, Nature, 420, 151

Secchi, P. A. 1870, Le Soleil, Gauthier Villars, Paris (p. 197).

Six, M. 1989, The Sun, Springer-Verlag, New York

Tandberg-Hanssen, E., Martin, S. F., and Hansen, R. T. 1980, Sol. Phys., 65, 357

Vernazza, J. E., Avrett, E. H., & Loeser, R. 1981, ApJ Supp. Series, 45, 635

Yoshida, T., & Tsuneta, S 1996, ApJ, 459, 342

FIGURE CAPTIONS

Fig. 1.—The multiple-turn helix in the X3 flare of 2002 July 15. The helix arises from sheared magnetic field along the neutral line between two flare ribbons at the feet of the helix. The emission is from CIV. The TRACE 160nm image has a field of view of 125 arcsec located between the positive sunspots (P_1 & P_3, see Figure 2) of active region AR10030. The eruption starts at ~20:04:17 UT and accelerates at 25 km s^{-1} during the first 30 s. The helix clearly has three turns at 20:04:51 UT, and these are seen earlier in the eruption (see white arrows at 20:04:34 UT)   In the movie version of this eruption containing 39 frames taken every two seconds, both legs of the loops are seen with the leg to the southwest showing an untwisting action. The base length of the helix is $3.9\text{x}10^4$ km as measured from foot to foot. From 20:04:51 UT, the loop begins to disappear and identification of the turns is impossible. A simple model of an erupting helix of 3 turns simulates the observed helix during time period of 20:04:23-20:04:51 UT. Shown with the same appropriate aspect angle of the CIV observations of the helix eruption, this simulation has the bowed helix core rising with each leg of the flux tube fixed to a 'photospheric' foot point.   An unwinding model can reproduce the spinning motion of the legs of the helix, as seen in the southwestern leg of the TRACE helix.

Fig. 2. — Upper panel: An MSFC vector magnetogram of AR 10030 showing the nonpotential field along the three main neutral line segments L_a, L_b and L_c. The magnetic contour levels are $\pm$ 2000, 1500, 1250, 1000, 200, 50, 0 G. The transverse field vectors are shown as dashes. The magnetic field along these neutral line segments is strongly sheared, having departure angles from the potential field greater than 45 degree (Falconer, Moore, & Gary, 2002). The photospheric brightness is the background image. The images of Figure 1 are about a fourth the width of this magnetogram and center on F_1. Lower panel: A high-resolution MDI magnetogram (10:56 UT) showing the principle sunspots, magnetic islands, and neutral lines. The small bipolar delta region (P_2 & F_2) developed during the day of July 15. The second, lower sunspot of P_3, moved rapidly (0.19 km s^{-1}) to the west during the day, with respect to the main spot of P_3. The MDI image magnetograms show motion of F_3 to the east. The motion within the complex continuously changes the stressed global magnetic field. The field of view is 4.'35 x 8.'72.

Fig. 3.—SOON Learmonth/SEC Hα image showing the filaments associated with neutral line segments L_a, L_b and L_c at 5:42 UT. The continuous neutral line (white line) is obtained from the high-resolution MDI magnetogram (Figure 2).

Fig. 4. —TRACE 160 nm images of key events in the X3 flare. At 19:49:58 and 20:02:53 UT the emission patches E_1, E_2, E_3, & E_4 are located at separatrix sites. The first eruption produces the two flare ribbons R_1 (shown at 20:05:02 UT) across the sheared-field neutral line L_b.   At 20:26:01, a second eruption produces the two flare ribbons R_2 across the sheared-field neutral line L_c. At 20:28:41, an upper atmospheric coronal separatrix (S) is seen. From the movie it is clear that this feature is located in the low corona.. In the later phase of the flare, at 20:41:58 UT, re-closing reconnection of the field again brightens separatrix sites E'_1 and E'_4. The thin line is the main neutral line from Figure 2.

Fig. 5. —Velocity profiles of the erupting helix. The transverse velocity (solid upper curve), as seen in the image plane, initially has a constant acceleration (dash-dotted line) of ~25 km s^{-1}. The measured transverse velocity is that of the top of the core of the helix. The radial expansion of the helix from its core has a velocity of ~185 km s^{-1} after about 15 seconds. The radial expansion was measured using the average semi-diameter of the main turns. Extrapolation of the transverse velocity to zero gives an onset time of t(0)= 20:04:17 UT. The times of the last 5 images of Figure 1 are marked A-E. At the time of each image, the vertical lines are the error (200 km s^{-1}) associated with the transverse velocity; the helix expansion velocity has the same uncertainty.

Fig. 6. —Side view and top view of potential field computed from an MDI magnetogram. The white set of field lines is associated with the negative flux F_1. The outer extremities of this set of field lines define the separatrix cupola. The small magnetic delta dipole (P_2 & F_2) hardly perturbs the overall quadrupolar field. The height in the side view is 140 Mm. At this height the plasma beta is ~1 (Gary 2001). Hence, the magnetic field is influenced by the (unknown) upper boundary conditions and this current-free field calculation models only the general connectivity to be expected, i.e., the topology. The helicity, the exact conjugate footpoints, and the upper boundary conditions of the region are not modeled.

Fig. 7. —Time profiles of the GOES X-ray flux in the 0.1-0.8 nm and 0.05-0.4 nm bands (Δt=1 min) and the OVSA 10 GHz microwave power (Δt=8 sec). The peaks in the X-ray profiles are at g_1=20:07 (X3.1) and g_2=20:28 (M4.1), and the peak in the radio profile are at r_1=20:03:52, r_2=20:11:20, and r_3=20:24:12. The microwave bursts have a FWHM~2-4 min. A reference line (dashed) is drawn at 20:04:00 UT.

Fig. 8.—Double CME event of July 15 20:30UT produced in tandem with the X3 X-ray flare. Although classified as a halo event, bright fronts are seen in the northeast; the active region location was N22 and E01. The first CME, the weaker of the two, is seen in the top row of panels and the strong second CME is seen in the bottom row. The full halo of the second CME was observed by 22:06UT, however the emission was fainter in the south. The second CME had a fast speed of ~1100 km s^{-1}. In the last panel, a difference image shows the second CME as seen by LASCO C3 at 02:18 UT on July 16. The weak halo in the southeast is seen opposite the main emission in the northeast. The images in the first five panels are nondifferenced LASCO C2 images.

Fig. 9. — Topological sketches of the main components of the eruption, shown in cross section for the quadrupolar sunspot configuration of AR 10030. These six panels represent the magnetic field configuration at times near or between the times of the TRACE images of Figure 4. In panel (1) the preflare magnetic field configuration is shown for t~19:50UT. The X-point null is the site of the initial breakout reconnection that unleashes the eruption of the sheared field along the neutral line L_b. The dots at this X-point indicate which field lines are reconnecting. In panel 2, the first breakout eruption is seen at t~20:05UT. In panel 3 the flare ribbons R_1 are shown with the associated open field lines at t~20:10UT. In panel 4 the re-closed field is shown with the dots for the next

breakout reconnection shown near the X-point at t~20:15UT. Panel 5 shows the flare ribbons R_2 associated with the field closing behind the second breakout event. In the last panel (6), the final-phase of the reclosing is shown at t~20:41UT with the emission at E'_1 and E'_4 from the reconnection above the Y-point. These illustrations show the flux F_1 larger than in actuality to make the X-point null above the region more obvious.

Fig. 10.— Left: An enlargement of the TRACE image at 20:28:41 UT extracted from Figure 3. The separatrix feature seen here is in the Y-null in the wake of the second eruption. (A separatrix refers to a magnetic surface across which linkage of field lines is discontinuous.) This region filled with material in the eruption leading to the two flare ribbons, seen here below the separatrix. Right: An illustration of the set of field lines defining the separatrix.
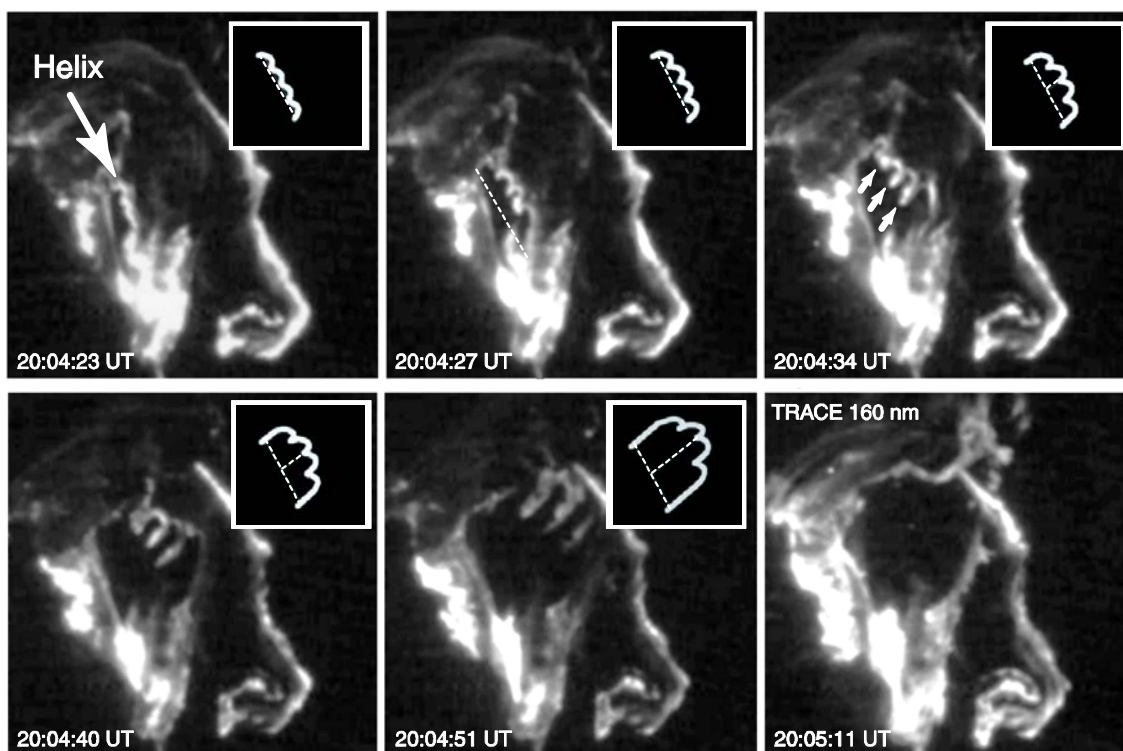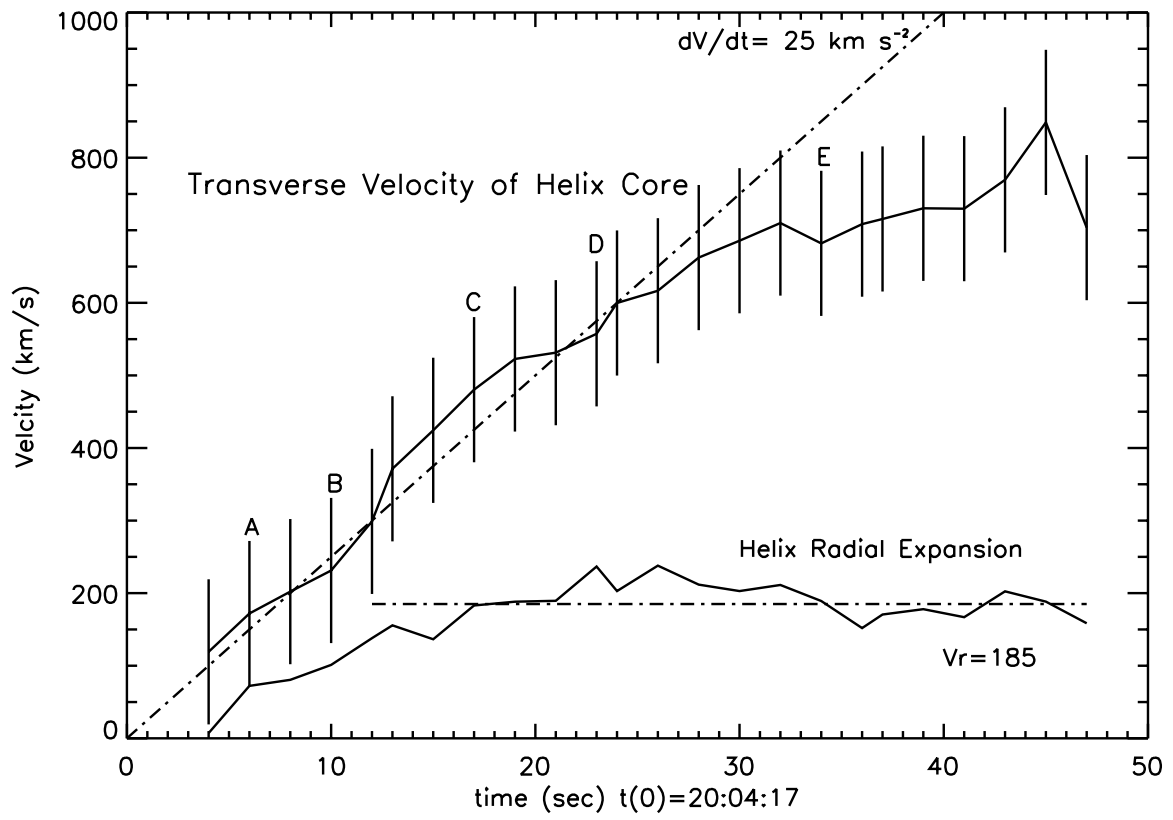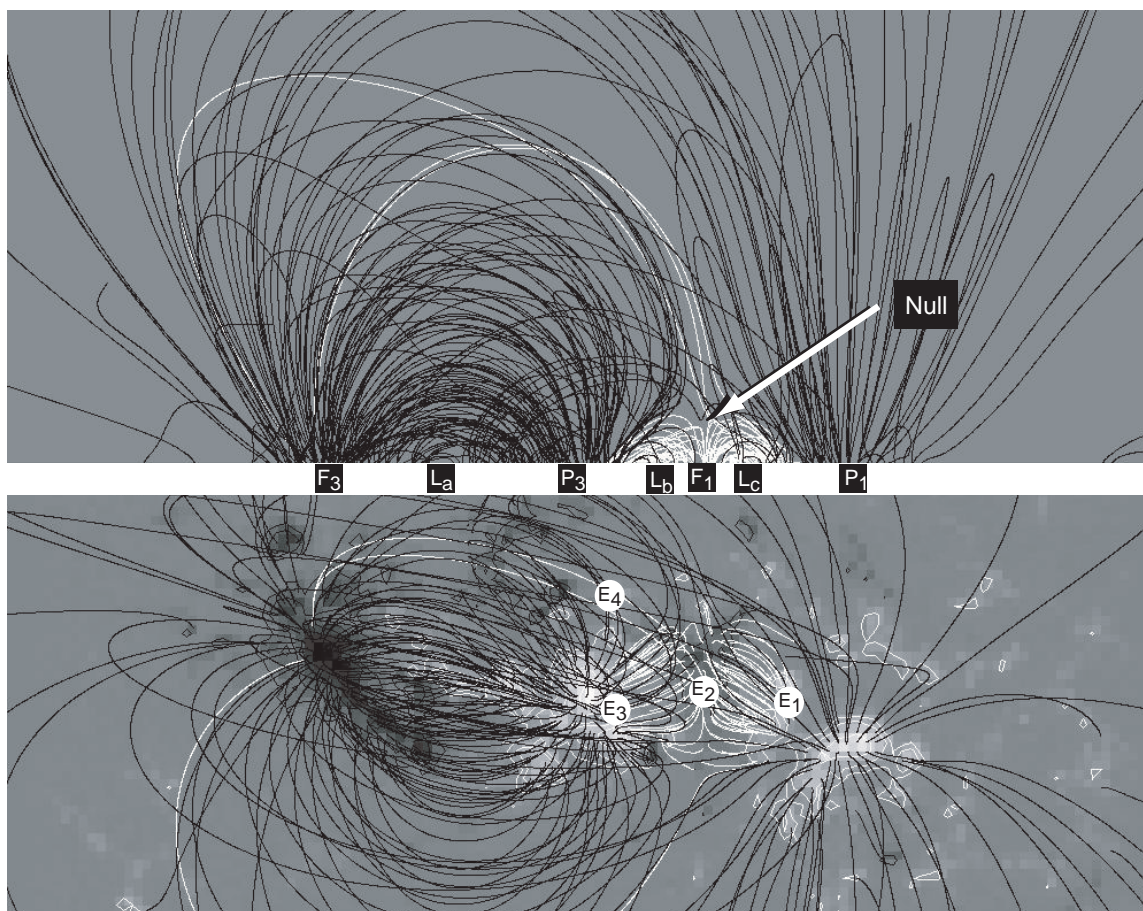
Figure 1.
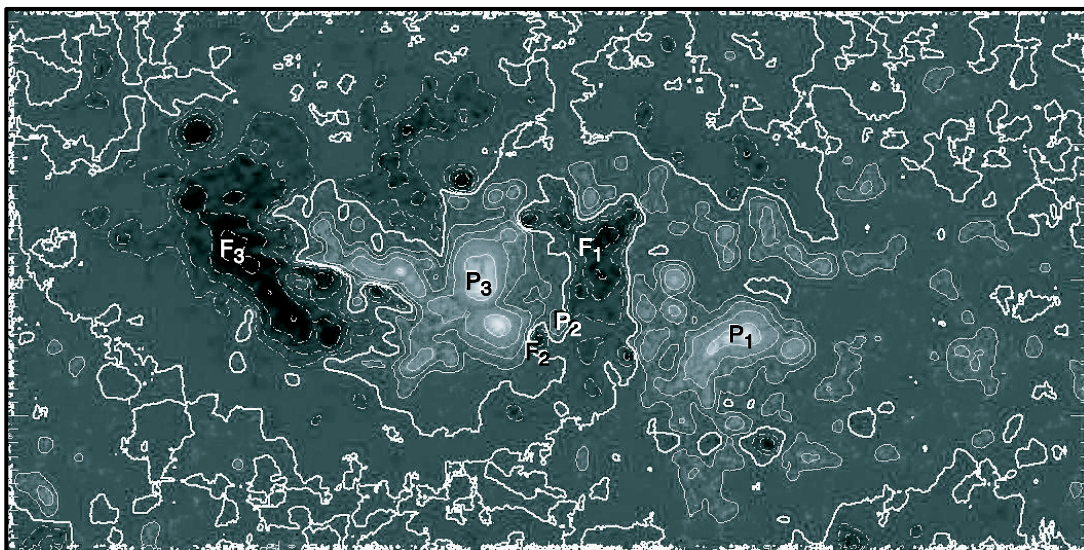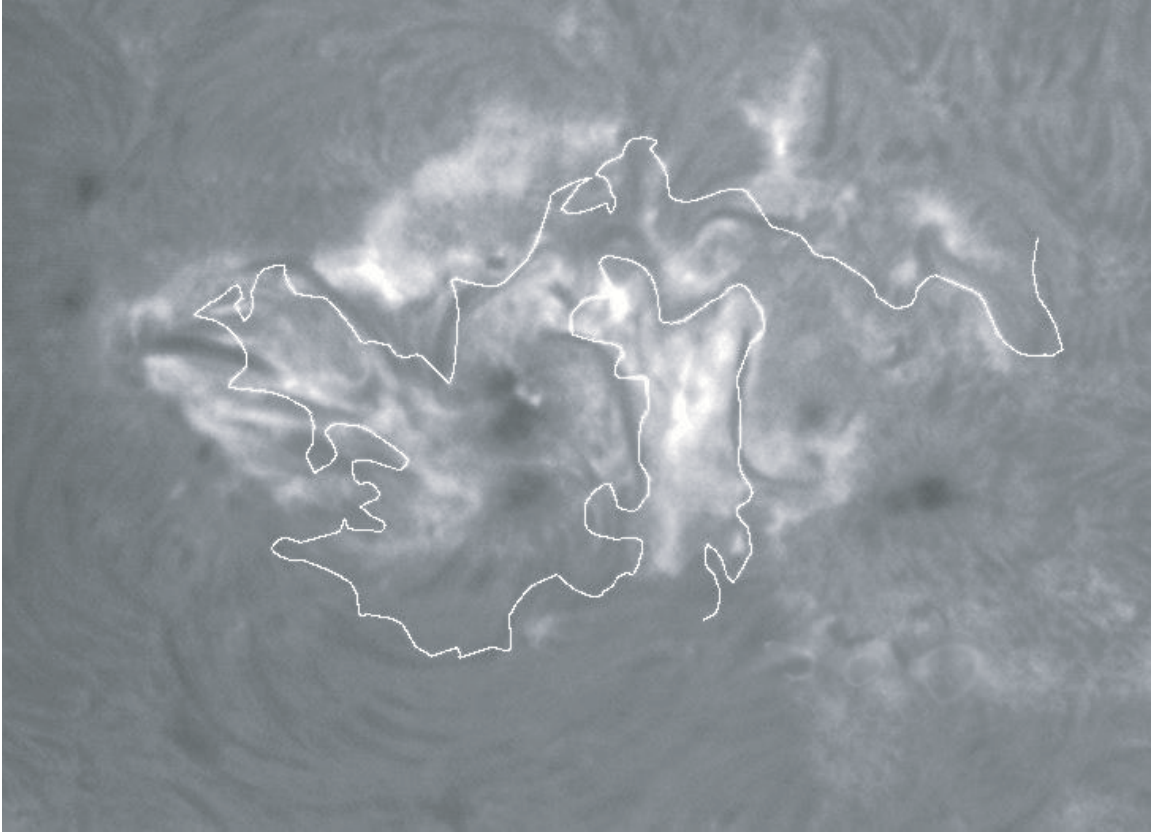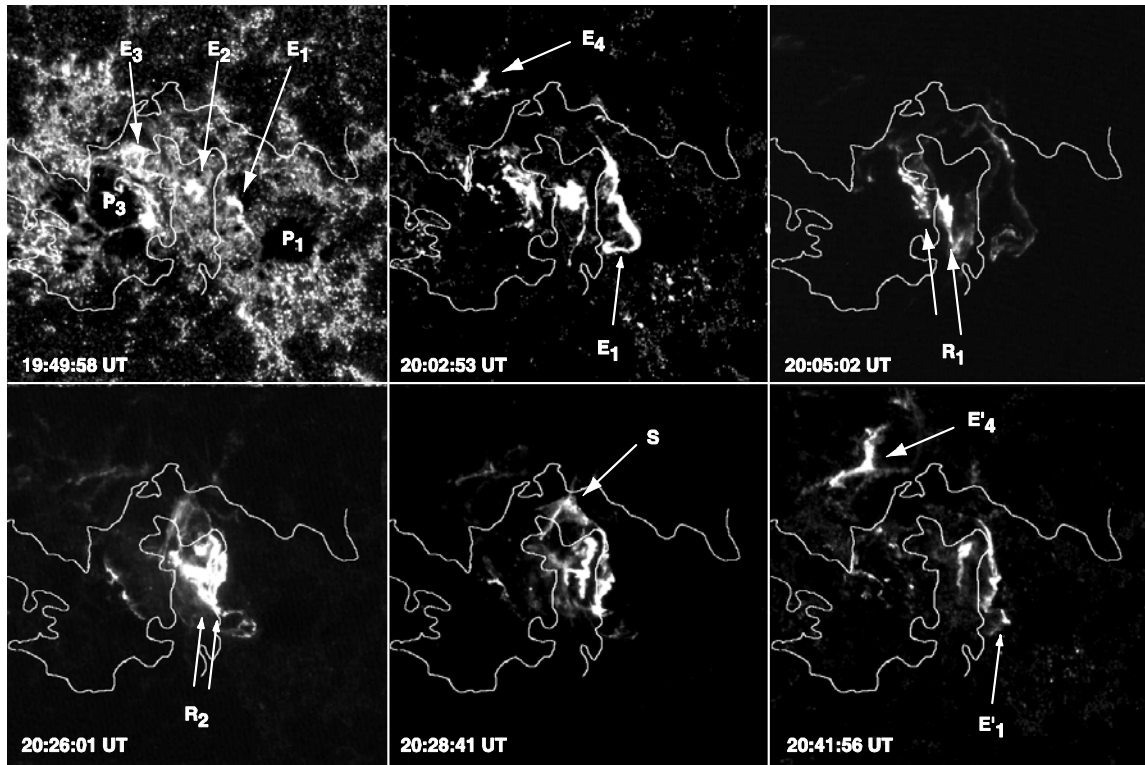
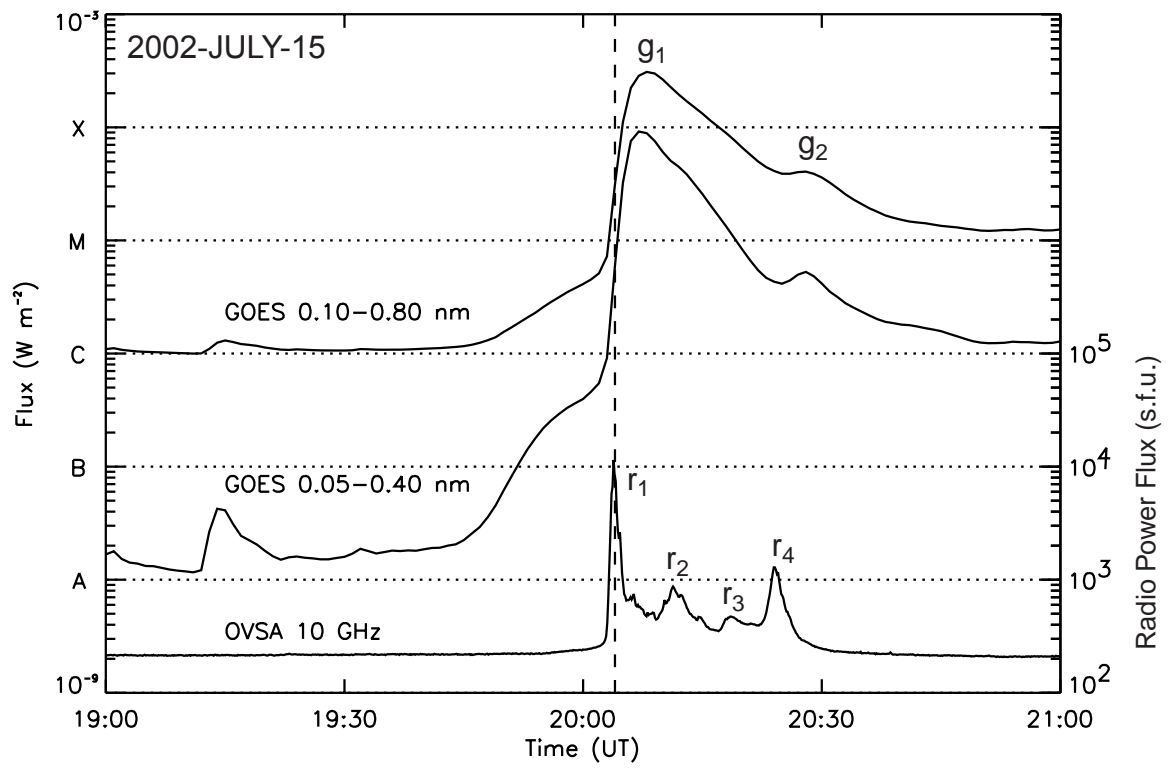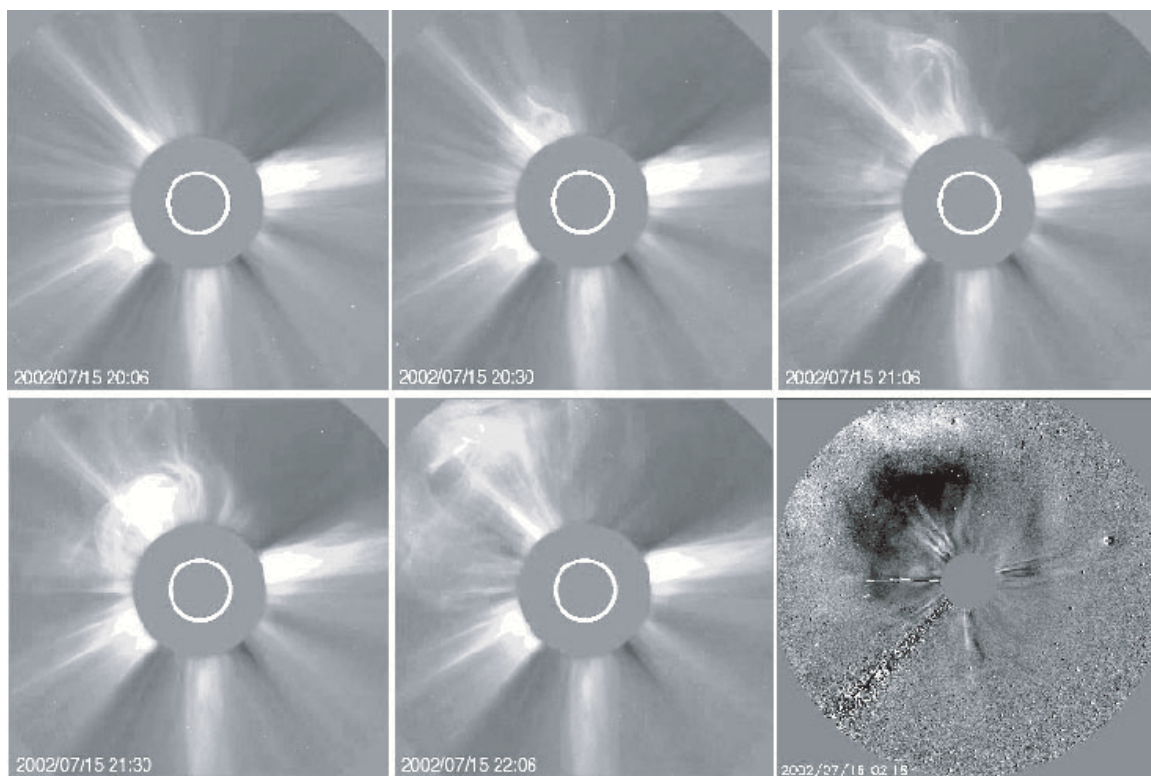Figure 2.

Figure 3.

Figure 4.

Figure 5.

Figure 6.

Figure 7.

Figure 8.

Figure 9.

TRACE 160 nm

20:28:41 UT

Rigid of the
Separatrix

S

Flare Ribbons R2

Figure 10.